NeuroImage: Clinical 19 (2018) 901–910

Contents lists available at ScienceDirect

NeuroImage: Clinical

journal homepage: www.elsevier.com/locate/ynicl

# Functional and structural brain networks in posterior cortical atrophy: A two-centre multiparametric MRI study

Federica Agosta[a,1], Gorana Mandic-Stojmenovic[a,c,1], Elisa Canu[a], Tanja Stojkovic[c], Francesca Imperiale[a], Francesca Caso[b], Elka Stefanova[c], Massimiliano Copetti[d], Vladimir S. Kostic[c], Massimo Filippi[a,b,*]

[a] Neuroimaging Research Unit, Institute of Experimental Neurology, Division of Neuroscience, San Raffaele Scientific Institute, Vita-Salute San Raffaele University, via Olgettina 60, 20132 Milan, Italy
[b] Department of Neurology, Institute of Experimental Neurology, Division of Neuroscience, San Raffaele Scientific Institute, Vita-Salute San Raffaele University, via Olgettina 60, 20132 Milan, Italy
[c] Clinic of Neurology, University of Belgrade, Dr Subotića 6, PO, Box 12, 11129, Belgrade 102, Serbia
[d] Biostatistics Unit, IRCCS-Ospedale Casa Sollievo della Sofferenza, Viale Cappuccini, San Giovanni Rotondo 71013, Foggia, Italy

ARTICLE INFO

*Keywords:*
Posterior cortical atrophy
White matter
Diffusion tensor MRI
Resting state functional connectivity
Default mode network
Visual network

ABSTRACT

This study identified structural and functional brain connectivity alterations in two independent samples of patients along the posterior cortical atrophy (PCA) disease course. Twenty-one PCA patients and 44 controls were recruited from two expert centres. Microstructural damage of white matter (WM) tracts was assessed using probabilistic tractography; resting state (RS) functional connectivity of brain networks was explored using a model free approach; grey matter (GM) atrophy was investigated using voxel-based morphometry. Compared with controls, common patterns of damage across PCA patients included: GM atrophy in the occipital-temporal-parietal regions; diffusion tensor (DT) MRI alterations of the corpus callosum and superior (SLF) and inferior longitudinal fasciculi (ILF) bilaterally; and decreased functional connectivity of the occipital gyri within the visual network and the precuneus and posterior cingulum within the default mode network (DMN). In PCA patients with longer disease duration and greater disease severity, WM damage extended to the cingulum and RS functional connectivity alterations spread within the frontal, dorsal attentive and salience networks. In PCA, reduced DMN functional connectivity was associated with SLF and ILF structural alterations. PCA patients showed distributed WM damage. Altered RS functional connectivity extends with disease worsening from occipital to temporo-parietal and frontostriatal regions, and this is likely to occur through WM connections. Future longitudinal studies are needed to establish trajectories of damage spreading in PCA and whether a combined DT MRI/RS functional MRI approach is promising in monitoring the disease progression.

## 1. Introduction

Posterior cortical atrophy (PCA) is a rare neurodegenerative syndrome characterized by a prominent progressive impairment of higher visual functions, such as disturbances on recognizing, locating and/or reaching objects under visual guidance, but also on a broad range of other cognitive domains subtended by occipito-temporal (ventral), occipito-parietal (dorsal), primary visual (caudal) or dominant parietal cerebral pathways (Crutch et al., 2017).

*In vivo* biomarker and postmortem pathological data indicate that the vast majority of reported cases of PCA are attributable to Alzheimer's disease (AD) (Alladi et al., 2007; Seguin et al., 2011; Tang-Wai et al., 2004). Unlike classic-amnestic AD, age at disease onset in PCA patients tends to be much earlier (from mid-50s to early 60) along with a relatively spared episodic memory (Borruat, 2013; Crutch et al., 2012).

In accordance with their clinical and neuropsychological features, magnetic resonance imaging (MRI) and 2-fluoro-2-deoxy-D-glucose (FDG) positron emission tomography (PET) studies in PCA patients have shown patterns of grey matter (GM) loss (Lehmann et al., 2011; Migliaccio et al., 2009; Whitwell et al., 2007) and glucose hypometabolism (Nestor et al., 2003; Whitwell et al., 2017) predominantly in

* Corresponding author at: Neuroimaging Research Unit, Institute of Experimental Neurology, Division of Neuroscience, San Raffaele Scientific Institute, Vita-Salute San Raffaele University, Via Olgettina, 60, 20132 Milan, Italy.
*E-mail address:* filippi.massimo@hsr.it (M. Filippi).
[1] These authors contributed equally to this work.

https://doi.org/10.1016/j.nicl.2018.06.013
Received 1 February 2018; Received in revised form 7 May 2018; Accepted 12 June 2018
Available online 12 June 2018

visual association areas (involving mainly the occipito-parietal and occipito-temporal cortices). Diffusion tensor (DT) MRI studies have shown that PCA is also associated with degeneration of white matter (WM) long-distance tracts connecting the occipito-parietal to the temporal and frontal brain regions (Caso et al., 2015; Madhavan et al., 2016; Migliaccio et al., 2012b; Migliaccio et al., 2012c). A model in which neurodegeneration in PCA selectively targets both posterior regions of the default mode network (DMN) and the visual network has been proposed (Lehmann et al., 2013; Ossenkoppele et al., 2015), although spatiotemporal trajectories of neurodegeneration are still not fully understood. Recent resting state functional MRI (RS fMRI) studies comparing small PCA samples with healthy controls reported altered higher visual network functional connectivity, while DMN findings were less consistent (Lehmann et al., 2015; Migliaccio et al., 2016).

In the present cross-sectional study, we sought to identify structural and functional brain connectivity alterations in two independent samples of patients along the PCA disease course. Patterns of GM atrophy were also explored. Assessing brain network abnormalities in patients with disparate clinical symptoms would help elucidating patterns of disease spread.

## 2. Methods

### 2.1. Participants

Twenty-one patients with a diagnosis of PCA (Crutch et al., 2017; Mendez et al., 2002) and 44 age-matched healthy controls were consecutively recruited at the Clinic of Neurology, Faculty of Medicine, University of Belgrade, Belgrade, Serbia (Sample#1: 8 PCA patients and 21 healthy controls) and the Department of Neurology, San Raffaele Scientific Institute, Milan, Italy (Sample#2: 13 PCA patients and 20 healthy controls). Ten of the 13 PCA patients of Sample#2 have been previously reported (Caso et al., 2015). This prior article dealt with structural MRI abnormalities in early onset AD variants, whereas in this manuscript we report on the patterns of structural and functional brain connectivity alterations in two independent samples of PCA patients. According to established criteria (Crutch et al., 2017; Mendez et al., 2002), diagnoses were based on a comprehensive evaluation including clinical history, neurological examination, and neuropsychological testing. Experienced neurologists blinded to the MRI results performed clinical assessments. History was taken with a structured interview from patients' relatives. Eligibility criteria included: no family history of dementia; no significant medical illnesses or substance abuse that could interfere with cognitive functioning; no any major systemic, psychiatric or (other) neurological illnesses; and absence of other causes of focal or diffuse brain damage, including lacunae and extensive cerebrovascular disease at routine MRI. When available, clinical diagnoses were supported by FDG PET (6 cases in Sample#1; 9 cases in Sample#2) and/or cerebrospinal fluid biomarkers (3 cases in Sample#1; 9 cases in Sample#2). All patients had an AD-like biomarker profile. Healthy controls with no history of neurologic, psychiatric or major medical illnesses were recruited among friends and spouses of patients and by word of mouth. This study was approved by the Local Ethical Committee on human studies and written informed consent from all subjects was obtained prior to their enrolment.

### 2.2. Neuropsychological assessment

In each centre, neuropsychological and behavioral evaluations were completed within 48 h of MRI by an experienced neuropsychologist, who was unaware of the MRI data. Full details are provided in the Supplementary Material.

### 2.3. MRI acquisition

Sample#1. MRI scans were obtained on a 1.5 Tesla Philips Medical System Achieva.

The following sequences were acquired: (i) dual-echo turbo (DE) spin-echo (repetition time [TR] = 3125 ms, echo time [TE] = 20/100 ms, echo train length = 6, 44 axial slices, thickness = 3 mm with no gap, matrix size = 256 × 247, field of view [FOV] = 240 × 232 $mm^2$); (ii) three-dimensional (3D) sagittal T1-weighted Turbo Field Echo (TFE) (frequency direction = anterior-posterior; TR = 7.1 ms, TE = 3.3 ms, inversion time [TI] = 1000 ms, flip angle = 8°, matrix size = 256 × 256 × 180 [inferior-superior, anterior-posterior, left-right], FOV = 256 × 256 $mm^2$); (iii) pulsed gradient SE single shot echo planar (EP) (TR = 6715 ms, TE = 86 ms, flip angle = 90°, matrix size = 112 × 110, FOV = 224 × 220 $mm^2$; 50 axial slices, thickness = 2.6 mm with no gap), with diffusion-encoding gradients applied in 65 non-collinear directions, selected as the default in the scanner (b factor = 1000 s/$mm^2$; seven averages). The maximum amplitude of the diffusion gradients was 33 mT/m and a multiple channel head coil was used for signal reception; and (iv) gradient-echo (GRE) EP imaging (EPI) sequence for RS fMRI (TR = 3000 ms, TE = 35 ms, flip angle = 90°, matrix size = 128 × 128, FOV = 240 × 240 $mm^2$; slice thickness = 4 mm, 200 sets of 30 contiguous axial slices). Total acquisition time of RS fMRI was about 12 min. During scanning, subjects were instructed to remain motionless and to keep their eyes closed.

Sample#2. MRI scans were obtained on a 3.0 T Philips Medical Systems Intera machine. The following sequences were acquired: (i) T2-weighted spin echo (SE) (TR = 3000 ms, TE = 85 ms, flip angle = 90°, echo train length = 15, thickness = 3 mm, 46 contiguous axial slices, FOV = 230 × 208 $mm^2$, matrix size = 256 × 242); (ii) fluid-attenuated inversion recovery (FLAIR) (TR = 11,000 ms, TE = 120 ms, inversion time = 2800 ms, flip angle = 90°, echo train length = 21, thickness = 3 mm, 46 contiguous axial slices, FOV = 230 × 183 $mm^2$, matrix size = 256 × 192); (iii) 3D T1-weighted fast field echo (TR = 25 ms, TE = 4.6 ms, flip angle = 30°, thickness = 1 mm, 220 contiguous axial slices, and in-plane resolution 0.89 × 0.89 $mm^2$, FOV = 230 × 230 $mm^2$, matrix size = 256 × 256,); (iv) pulsed-gradient SE EP with sensitivity encoding (acceleration factor = 2.5, TR = 8986 ms, TE = 80 ms, thickness = 2.5 mm, 55 contiguous axial slices number of acquisitions = 2; FOV = 240 × 240 $mm^2$, acquisition matrix = 96 × 96, in-plane pixel size 0.94 × 0.94 $mm^2$), with diffusion-encoding gradients applied in 32 non-collinear directions, using a gradient scheme which is standard on this system (gradient over-plus) and optimized to reduce echo time as much as possible (b factor = 1000 s/$mm^2$); and (v) T2*-weighted single-shot EPI sequence for RS fMRI (TR = 3000 ms, TE = 35 ms, flip angle = 90°, matrix size = 128 × 128, FOV = 240 × 240 $mm^2$; slice thickness = 4 mm, 200 sets of 30 contiguous axial slices). Total acquisition time of RS fMRI was about 10 min. During scanning, subjects were instructed to remain motionless and to keep their eyes closed.

### 2.4. MRI analysis

An experienced observer, blinded to patients' identity, performed MRI analysis. Briefly, GM atrophy was investigated using voxel-based morphometry (VBM) in SPM12; microstructural damage of WM tracts was assessed using DT MRI and probabilistic tractography in FSL; RS functional connectivity of brain networks was explored using a model free approach in FSL (MELODIC).

#### 2.4.1. GM atrophy: voxel-based morphometry

VBM was performed using SPM12 and the Diffeomorphic Anatomical Registration Exponentiated Lie Algebra (DARTEL) registration method (Ashburner, 2007). Briefly, (i) T1-weighted images were segmented to produce GM, WM and cerebrospinal fluid (CSF) tissue probability maps in the Montreal Neurological Institute (MNI) space; (ii) the segmentation parameters obtained from the step (i) were imported in DARTEL; (iii) the rigidly aligned version of the images

previously segmented (i) was generated; (iv) the DARTEL template was created and the obtained flow fields were applied to the rigidly-aligned segments to warp them to the common DARTEL space and then modulated using the Jacobian determinants. Since the DARTEL process warps to a common space that is smaller than the MNI space, we performed an additional transformation as follows: (v) the modulated images from DARTEL were normalized to the MNI template using an affine transformation estimated from the DARTEL GM template and the a priori GM probability map without resampling (http://brainmap.wisc.edu/normalizeDARTELtoMNI). Prior to statistical computations, images were smoothed with an 8 mm FWHM Gaussian filter.

#### 2.4.2. WM tracts: tractography

The diffusion-weighted data were skull-stripped using the Brain Extraction Tool (BET) implemented in FSLv5.0 (http://fsl.fmrib.ox.ac.uk/fsl). In Sample#1, the diffusion-weighted images (DWI) were corrected for distortions caused by eddy currents and movements, using an implementation of the algorithm described in Rohde et al., 2004 (Rohde et al., 2004) (http://white.stanford.edu/newlm/index.php/DTI_Preprocessing#dti Raw_Preprocessing_Pipeline). This eddy-current/motion correction step combines a rigid-body 3D motion correction (6 parameters) with a constrained non-linear warping (8 parameters) based on a model of the expected eddy-current distortions. In Sample#2, using FMRIB's Linear Image Registration Tool (FLIRT), the two diffusion-weighted scans were coregistered by applying the rigid transformation needed to correct for position between the two $b_0$ images (T2-weighted, but not diffusion-weighted). The rotation component was also applied to diffusion-weighted directions. Eddy currents correction was performed using the JIM5 software. Then, the two acquisitions were concatenated.

In both Samples, the DT was estimated on a voxel-by-voxel basis using the DTIfit toolbox, part of the FMRIB Diffusion Toolbox within FSL, in order to obtain fractional anisotropy (FA), mean (MD), axial (axD) and radial diffusivities (radD) maps.

Seeds for tractography of the cingulum, corpus callosum (CC-whole tract, genu, body and splenium), superior longitudinal (SLF), inferior longitudinal (ILF), and uncinate fasciculi were defined in the MNI space on the FA template provided by FSL, as previously described (Canu et al., 2015). Fiber tracking was performed in native DT MRI space using a probabilistic tractography algorithm implemented in FSL (probtrackx), which is based on Bayesian estimation of diffusion parameters (Bedpostx) (Behrens et al., 2007). Fiber tracking was initiated from all voxels within the seed masks in the diffusion space to generate 5000 streamline samples with a step length of 0.5 mm and a curvature threshold of 0.2. Tract maps were then normalized taking into consideration the number of voxels in the seed masks. To this aim, the number of streamlines present in the voxels of the tract maps was divided by the way-total, which corresponds to the total number of streamlines that were not rejected by the exclusion masks. The tract masks obtained were thresholded at a value equal to 40% of the 95th percentile of the distribution of the intensity values of the voxels included in the tract. This normalization procedure allowed to correct for possible differences between tracts due to the different sizes of the starting seeds. In this way, we also excluded the background noise and avoided a too restrictive thresholding when the maximum intensity value was an outlier. Using a “seed” approach, the reconstructions of the tracts of interest were obtained. For each tract, the average FA, MD, axD and radD were calculated in the native space.

#### 2.4.3. RS functional connectivity

In both samples, FMRI analysis was performed using FSL (FSLv5.0). Preprocessing was performed using FEAT (Jenkinson et al., 2012; Smith et al., 2004; Woolrich et al., 2009) and included: (i) removal of the first four volumes to allow for signal equilibration; (ii) head movement correction by volume-realignment to the middle volume using MCFLIRT; (iii) global 4D mean intensity normalization; and (iv) spatial smoothing (5 mm FWHM). We then applied ICA-AROMA (Independent Component Analysis-based Automatic Removal Of Motion Artifacts) (Pruim et al., 2015) in order to identify those independent components (ICs) representing motion-related artifacts. This method calculates a set of spatial and temporal discriminative features and, according to them, exploits a classification procedure to identify ICs representing motion artifacts. Specifically, these features evaluate the spatial overlaps of each component with the edges of brain and CSF, and the frequency content and the temporal correlation with realignment parameters of the IC time-series. Finally, ICs classified as motion-related were removed from the fMRI dataset by means of linear regression. Resulting fMRI dataset was then high-pass filtered (cut-off frequency of 0.01 Hz) and co-registered to the participant's 3D T1-weighted TFE image using affine boundary-based registration as implemented in FLIRT (Greve and Fischl, 2009; Jenkinson and Smith, 2001), and subsequently transformed to the MNI152 standard space with 4 mm isotropic resolution using non-linear registration through FNIRT (Andersson et al., 2007). Pre-processed fMRI data, containing 196 time-points for each subject, were temporally concatenated across subjects to create a single 4D dataset. This FMRI dataset was then decomposed into ICs with a free estimation for the number of components using MELODIC (Multivariate Exploratory Linear Optimized Decomposition into Independent Components) (Beckmann et al., 2005).

### 2.5. Statistical analysis

#### 2.5.1. Demographic, clinical and cognitive data

Group comparisons of continuous variables were performed using ANOVA models, followed by post-hoc pairwise comparisons (SAS Release 9.3, SAS Institute, Cary, NC, USA).

#### 2.5.2. Voxel-based morphometry

Analyses of covariance were performed to assess GM volume differences between each PCA patient group and age-matched healthy controls. Total intracranial volume and age at the MRI were included in the models as covariates. The statistical threshold was set at $p < 0.05$ Family-wise error (FWE)-corrected within at least 20 contiguous voxels.

#### 2.5.3. DT MRI metrics of WM tracts

DT MRI measures of WM tracts of interest (cingulum, CC, SLF, ILF, uncinate fasciculus) were compared between groups using ANCOVA models, age and Bonferroni-corrected for multiple comparisons ($p < 0.05$; SAS Release 9.3).

#### 2.5.4. RS functional connectivity

Between-group analysis of the RS fMRI data was carried out using a dual-regression technique as implemented in FSL (Filippini et al., 2009), an approach that allows to identify subject-specific temporal dynamics and spatial maps that are associated with each group IC map. Among group-IC spatial maps, ICs of interest (DMN, visual network, left and right frontoparietal networks, frontal, salience, dorsal attentive networks) were selected by visual inspection based on previous literature (Smith et al., 2009) (Supplementary Figure). Then, dual-regression procedure was performed, which involves: (i) the use of the selected group-IC spatial maps in a linear model fit (spatial regression) against the single subject fMRI data sets, resulting in matrices describing temporal dynamics for each IC and subject; and (ii) the use of these time-course matrices which are entered into a linear model fit (temporal regression) against the associated fMRI data set to estimate subject-specific spatial maps (Filippini et al., 2009). After dual regression, spatial maps of all subjects were collected into single 4D files for each original IC. Nonparametric permutation tests (5000 permutations) were used to detect statistically significant differences between groups within the RSN of interest obtained with MELODIC (the single 4D files for each original IC) (Nichols and Holmes, 2002). Furthermore, analyses were corrected for GM segments, age and restricted within the spatial RS

**Table 1**
Demographic and clinical features of PCA patients and healthy controls.

| | Sample#1 | | | Sample#2 | | | |
|---|---|---|---|---|---|---|---|
| | PCA | HC | p | PCA | HC | p | p Between patient groups |
| Number | 8 | 24 | | 13 | 20 | | |
| Men/women (% men) | 5/3 (63%) | 14/10 (58%) | 0.84 | 4/9 (31%) | 7/13 (35%) | 0.80 | 0.15 |
| Age at MRI, years | 60.2 ± 4.7 (53–67) | 60.9 ± 6.7 (50–74) | 0.78 | 61.9 ± 6.0 (56–78) | 62.0 ± 2.8 | 0.97 | 0.50 |
| Education, years | 13.6 ± 2.3 (12–17) | 13.0 ± 3.1 (8–18) | 0.63 | 9.5 ± 3.2 (5–13) | 16.0 ± 4.7 | < 0.001 | 0.01 |
| Age at onset, years | 55.4 ± 4.8 (49–63) | – | – | 58.5 ± 6.6 (52–77) | – | – | 0.26 |
| Disease duration, years | 4.8 ± 1.6 (3–8) | – | – | 3.4 ± 1.1 (1–5) | – | – | 0.02 |
| CSF, $A\beta_{42}$* | 552.0 ± 229.0 (414–816) | – | – | 369.4 ± 180.4 (151–607) | – | – | – |
| CSF, T-Tau* | 502.7 ± 174.6 (391–704) | – | – | 339.0 ± 192.6 (80–644) | – | – | – |
| CSF, p-Tau* | 79.4 ± 12.6 (72–94) | – | – | 103.1 ± 100.9 (36–363) | – | – | – |
| CDR | 1.9 ± 0.9 (0.5–3) | – | – | 1.2 ± 0.4 (1–2) | – | – | 0.07 |
| CDR, SB | 10.9 ± 5.8 (0–18) | – | – | 5.4 ± 1.6 (4–8) | – | – | 0.07 |
| ADL | 34.8 ± 25.0 (0–70) | – | – | 5.3 ± 1.1 (3–6) | – | – | NC |

Values denote means ± standard deviations (range or frequencies). CSF normal values Sample#1: $A\beta_{42}$ > 563.1 ng/L; T-tau < 244.7 ng/L; p-Tau < 83.4 ng/L. CSF normal values Sample#2: $A\beta_{42}$ > 500 ng/L; T-tau < 450 ng/L; p-Tau < 61 ng/L.
Abbreviations: $A\beta_{42}$ = amyloid β 42; ADL = activities of daily living; CDR = clinical dementia rating scale; CSF = cerebrospinal fluid; HC = healthy controls; MRI = magnetic resonance imaging; NC = not comparable (different clinical scales); PCA = posterior cortical atrophy; p-tau = phosphorylated protein tau; SB = sum of boxes; T-tau = total tau. * = available for three patients from sample#1 and 9 from sample#2

network of interest using binary masks obtained by thresholding the corresponding Z map image (Z > 2.3). FWE correction for multiple comparisons was performed, implementing the Threshold-Free Cluster Enhancement method using a significance threshold of p < 0.05 (Smith and Nichols, 2009).

#### 2.5.5. Correlations

In PCA patients, correlations between clinical features, DT MRI measures, and RS functional connectivity findings were tested. Analyses were restricted to MRI metrics significantly different between patients and controls. Multiple regression models were Bonferroni-corrected for multiple comparisons (p < 0.05; SAS Release 9.3).

## 3. Results

### 3.1. Demographic, clinical and cognitive data

Groups were similar for age and gender. Sample#2 patients had less years of education than controls and Sample#1 patients (Table 1). PCA groups were similar for age at the disease onset, but Sample#1 had longer disease duration and a trend toward a greater disease severity compared to patients of Sample#2 (Table 1). Compared with controls, PCA patients performed worse in all investigated cognitive domains (Supplementary Tables 1 and 2). At the time of the visit, patients presented with ventral symptoms, such as visual agnosia (52%), prosopagnosia (57%), and alexia (86%); dorsal symptoms, such as neglect (24%), optic ataxia (38%), oculomotor apraxia (19%) and simultanagnosia (43%); Gerstmann's syndrome such as finger agnosia (52%), left and right disorientation (48%) and acalculia (66%); and other deficits such as apperceptive agnosia (71%), space perception and exploration (76%) and ideomotor limb apraxia (81%) (Table 2).

### 3.2. Voxel-based morphometry

The severity and regional distribution of GM loss in each patient group vs controls were consistent with those reported in the literature (Lehmann et al., 2011; Migliaccio et al., 2009; Whitwell et al., 2007) (Supplementary Table 3, Fig. 1). Briefly, regions of GM volume loss were detected in both PCA samples in the occipital (fusiform, inferior and middle occipital gyri, mainly at the right side), parietal (bilateral angular and middle cingulum), temporal (bilateral middle and inferior temporal gyri and hippocampus), and frontal (small clusters in the bilateral middle and inferior frontal gyri) cortices (Supplementary Table 3, Fig. 1), with a greater extent to the posterior brain regions.

### 3.3. WM tracts

Compared with controls, both PCA groups showed a pattern of WM damage involving the body and splenium of the CC, bilateral SLF and left ILF (Table 3, Fig. 1). Sample#1 showed further WM alterations in the bilateral cingulum and right ILF (Table 3, Fig. 1).

### 3.4. RS functional connectivity

Compared with healthy controls, each group of PCA patients showed common patterns of reduced RS functional connectivity in the left middle occipital gyrus within the visual I network and in the right posterior cingulum and precuneus within the DMN (Table 4, Fig. 2). In Sample#1 group compared with controls, reduced functional connectivity further extended to the bilateral calcarine cortex and cuneus within the visual I network and to the left middle temporal and occipital gyri within the DMN (Table 4, Fig. 2). Furthermore, Sample#1 compared with controls showed reduced RS functional connectivity in the left superior temporal gyrus, supramarginal gyrus and paracentral lobule within the dorsal attentive network; in the left thalamus and hippocampus within the salience network; and in the bilateral anterior cingulum and right medial superior frontal gyrus within the frontal network (Table 4, Fig. 2). No clusters of increased functional connectivity were observed in PCA patients relative to controls.

### 3.5. Correlations

In each patient group (separately), no correlation was found between MRI metrics and disease duration and severity. In Sample#1, reduced RS functional connectivity of the left middle occipital gyrus within the DMN was associated with right SLF alterations (increased MD: Spearman's rho = −0.92, p = 0.04). In Sample#2, reduced RS functional connectivity of the right precuneus within the DMN was associated with left ILF changes (increased MD: Spearman's rho = −0.78, p = 0.01; increased axD: Spearman's rho = −0.73, p = 0.04).

## 4. Discussion

In this study, we reported patterns of brain structural and RS functional connectivity features of two independent samples of PCA patients. Compared to healthy controls, both PCA groups showed damage of the CC, SLF and ILF, and decreased RS functional connectivity within the visual network and DMN. In PCA patients with longer

**Table 2**
Clinical features of each PCA patient from the two samples at the time of the MRI scan.

| | Sample#1 | | | | | | | | Sample#2 | | | | | | | | | | | | |
|---|---|---|---|---|---|---|---|---|---|---|---|---|---|---|---|---|---|---|---|---|---|
| Cases | 1 | 2 | 3 | 4 | 5 | 6 | 7 | 8 | 1 | 2 | 3 | 4 | 5 | 6 | 7 | 8 | 9 | 10 | 11 | 12 | 13 |
| Ventral symptoms | | | | | | | | | | | | | | | | | | | | | |
| Visual agnosia | | | + | | + | + | | + | + | | + | | | | | + | + | + | + | | + |
| Prosopoagnosia | + | + | | | | + | | + | | + | + | + | + | + | + | | | + | + | | |
| Alexia | + | + | + | + | + | + | + | + | + | | | + | | + | + | + | + | + | + | + | + |
| Dorsal symptoms | | | | | | | | | | | | | | | | | | | | | |
| Neglect | | | | | + | | | + | | | + | + | | | | | | + | | | |
| Optic ataxia | + | | | | | + | | + | + | + | | | | | | + | + | + | | | |
| Oculomotor apraxia | | | | | | + | | + | + | | | | | | | + | | | | | |
| Simultanagnosia | + | + | | | | + | | + | + | + | + | | | | | + | + | | | | |
| Gerstmann's syndrome | | | | | | | | | | | | | | | | | | | | | |
| Finger agnosia | + | + | | | | + | | | + | | + | | | + | + | + | | + | + | | + |
| L/R disorientation | | + | + | | + | + | + | | + | | | + | | + | + | | | + | | | |
| Acalculia | + | + | + | + | + | | + | | | + | + | + | | + | | | + | + | | + | + |
| Other deficits | | | | | | | | | | | | | | | | | | | | | |
| Apperceptive agnosia* | + | + | + | | + | + | | + | + | + | + | | + | | + | + | | + | + | | + |
| Space perception and exploration | + | + | + | + | + | + | + | + | + | | + | + | + | | + | | + | | + | + | |
| Ideomotor limb apraxia | + | + | + | + | + | | + | | + | + | + | | + | + | | + | + | + | + | + | + |

+ = deficit present at the time of the visit; * = difficulties in discriminating visual features; L/R = left and right.

disease duration and greater disease severity, WM damage extended to the cingulum and RS functional connectivity alterations spread within the frontal, dorsal attentive and salience networks. In line with previous studies (Lehmann et al., 2011; Migliaccio et al., 2009; Whitwell et al., 2007), we detected areas of GM volume loss in both PCA samples, with the greater extent to occipital-parietal and occipito-temporal cortices.

According with the clinical syndrome and previous studies (Caso et al., 2015; Madhavan et al., 2016; Migliaccio et al., 2012b; Migliaccio et al., 2012c), common WM damage across PCA groups were found in the ventral (ILF) and dorsal (SLF) structural visual pathways. In addition, PCA patients showed the involvement of the CC, which has been found to be a common target of pathology shared by syndromic variants of AD (Caso et al., 2015; Madhavan et al., 2016; Migliaccio et al., 2012a). Pathological studies in PCA patients, reporting pathological features of AD, showed the greatest density of senile plaques and neurofibrillary tangles in occipitoparietal cortices and posterior cingulate cortex (Hof et al., 1997; Levine et al., 1993; Tang-Wai et al., 2004). Thus, microstructural damage to the visual pathways and CC can be

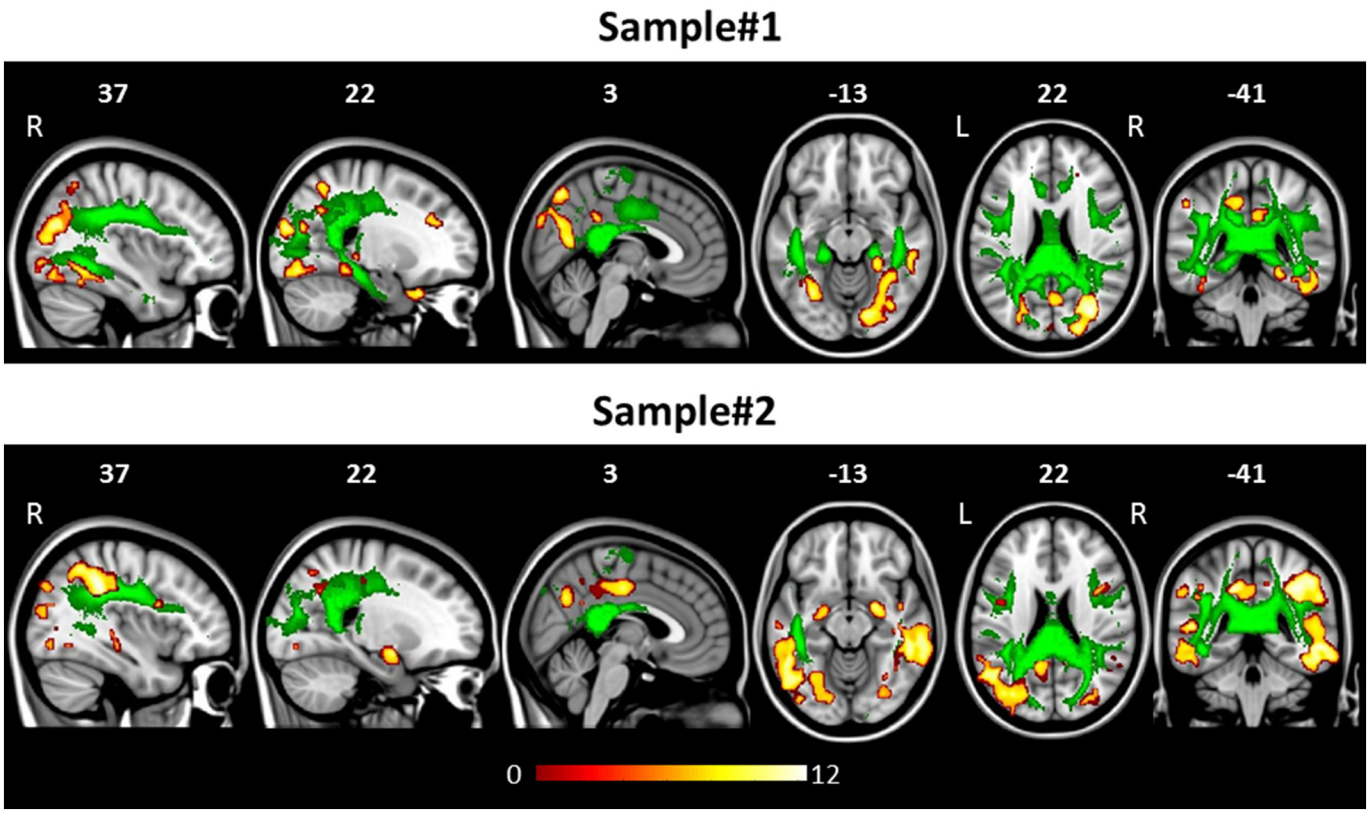


**Fig. 1.** Grey matter (GM) atrophy (warm colours) and white matter (WM) tract damage (green colour) in patients with posterior cortical atrophy compared with healthy controls accounting for age. Patterns of damage represent findings of voxel based morphometry for GM ($p < 0.05$ Family Wise Error-corrected within 20 contiguous voxels; coloured bars denote T values) and tractography for WM tracts ($p < 0.05$ Bonferroni-corrected for multiple comparisons). Results are overlaid on the Montreal Neurological Institute standard brain in neurological convention (right is right). L = left; R = Right.

**Table 3**
Diffusion Tensor MRI metrics of white matter tracts in PCA patients and healthy controls.

| | Sample#1 | | | | | | Sample#2 | | | | | |
|---|---|---|---|---|---|---|---|---|---|---|---|---|
| | FA | | | MD [$\times 10^{-3}$ mm$^2$ s$^{-1}$] | | | FA | | | MD [$\times 10^{-3}$ mm$^2$ s$^{-1}$] | | |
| Region | PCA | HC | p | PCA | HC | p | PCA | HC | p | PCA | HC | p |
| CC | 0.52 ± 0.02 (0.49–0.55) | 0.56 ± 0.02 (0.51–0.60) | < 0.001 | 1.02 ± 0.09 (0.93–1.17) | 0.92 ± 0.05 (0.84–1.01) | 0.03 | 0.47 ± 0.04 (0.43–0.52) | 0.50 ± 0.02 (0.46–0.54) | 0.60 | 1.01 ± 0.11 (0.83–1.15) | 0.87 ± 0.04 (0.82–0.94) | < 0.001 |
| CC Genu | 0.48 ± 0.03 (0.44–0.53) | 0.51 ± 0.02 (0.47–0.57) | 0.35 | 0.96 ± 0.08 (0.83–1.08) | 0.92 ± 0.07 (0.82–1.09) | 1.00 | 0.44 ± 0.04 (0.39–0.50) | 0.44 ± 0.02 (0.39–0.48) | 1.00 | 0.95 ± 0.10 (0.79–1.09) | 0.89 ± 0.06 (0.80–1.01) | 1.00 |
| CC Body | 0.49 ± 0.02 (0.46–0.52) | 0.53 ± 0.02 (0.50–0.58) | 0.003 | 1.00 ± 0.09 (0.91–1.18) | 0.91 ± 0.06 (0.82–1.01) | 0.08 | 0.45 ± 0.04 (0.39–0.51) | 0.47 ± 0.02 (0.43–0.52) | 1.00 | 1.01 ± 0.12 (0.82–1.23) | 0.85 ± 0.04 (0.79–0.95) | 0.001 |
| CC Splenium | 0.56 ± 0.02 (0.54–0.59) | 0.60 ± 0.02 (0.55–0.65) | < 0.001 | 1.09 ± 0.09 (1.00–1.25) | 0.93 ± 0.05 (0.86–1.02) | < 0.001 | 0.50 ± 0.03 (0.43–0.54) | 0.52 ± 0.02 (0.48–0.55) | 1.00 | 1.02 ± 0.12 (0.89–1.34) | 0.89 ± 0.04 (0.84–0.98) | 0.01 |
| L Cingulum | 0.39 ± 0.04 (0.32–0.43) | 0.42 ± 0.03 (0.38–0.51) | 0.50 | 0.89 ± 0.06 (0.84–0.97) | 0.83 ± 0.03 (0.75–0.88) | 0.03 | 0.35 ± 0.03 (0.30–0.39) | 0.36 ± 0.02 (0.32–0.40) | 1.00 | 0.87 ± 0.05 (0.82–0.97) | 0.83 ± 0.03 (0.78–0.91) | 0.86 |
| R Cingulum | 0.37 ± 0.03 (0.32–0.41) | 0.41 ± 0.03 (0.36–0.47) | 0.41 | 0.90 ± 0.07 (0.83–1.02) | 0.82 ± 0.03 (0.77–0.87) | 0.02 | 0.33 ± 0.03 (0.29–0.37) | 0.35 ± 0.02 (0.31–0.38) | 1.00 | 0.87 ± 0.06 (0.76–0.95) | 0.81 ± 0.03 (0.78–0.86) | 0.19 |
| L ILF | 0.43 ± 0.05 (0.32–0.48) | 0.46 ± 0.04 (0.38–0.52) | 1.00 | 0.91 ± 0.07 (0.81–1.04) | 0.83 ± 0.03 (0.78–0.90) | 0.01 | 0.43 ± 0.03 (0.39–0.49) | 0.43 ± 0.02 (0.38–0.49) | 1.00 | 0.89 ± 0.05 (0.84–0.99) | 0.83 ± 0.04 (0.76–0.90) | 0.02 |
| R ILF | 0.42 ± 0.04 (0.33–0.47) | 0.45 ± 0.05 (0.35–0.54) | 1.00 | 0.89 ± 0.03 (0.85–0.93) | 0.81 ± 0.04 (0.76–0.90) | < 0.001 | 0.42 ± 0.03 (0.34–0.47) | 0.43 ± 0.02 (0.38–0.47) | 1.00 | 0.88 ± 0.06 (0.82–0.98) | 0.83 ± 0.04 (0.77–0.90) | 0.65 |
| L SLF | 0.42 ± 0.03 (0.39–0.47) | 0.45 ± 0.04 (0.39–0.54) | 1.00 | 0.83 ± 0.04 (0.77–0.90) | 0.78 ± 0.03 (0.72–0.82) | 0.005 | 0.39 ± 0.03 (0.33–0.43) | 0.42 ± 0.02 (0.39–0.45) | 0.05 | 0.81 ± 0.04 (0.77–0.89) | 0.75 ± 0.03 (0.70–0.80) | < 0.001 |
| R SLF | 0.40 ± 0.03 (0.35–0.45) | 0.45 ± 0.03 (0.37–0.50) | 0.04 | 0.87 ± 0.05 (0.80–0.95) | 0.78 ± 0.03 (0.73–0.84) | < 0.001 | 0.37 ± 0.04 (0.30–0.44) | 0.40 ± 0.02 (0.37–0.44) | 0.14 | 0.83 ± 0.05 (0.77–0.93) | 0.77 ± 0.02 (0.73–0.80) | 0.003 |
| L UNC | 0.43 ± 0.04 (0.38–0.50) | 0.44 ± 0.03 (0.36–0.49) | 1.00 | 0.86 ± 0.02 (0.83–0.88) | 0.85 ± 0.04 (0.80–1.01) | 1.00 | 0.36 ± 0.04 (0.30–0.43) | 0.37 ± 0.03 (0.29–0.43) | 1.00 | 0.89 ± 0.06 (0.80–0.98) | 0.85 ± 0.04 (0.78–0.95) | 0.39 |
| R UNC | 0.42 ± 0.03 (0.38–0.47) | 0.43 ± 0.07 (0.23–0.52) | 1.00 | 0.86 ± 0.04 (0.81–0.93) | 0.84 ± 0.05 (0.76–0.94) | 1.00 | 0.37 ± 0.02 (0.31–0.39) | 0.38 ± 0.03 (0.34–0.42) | 1.00 | 0.88 ± 0.06 (0.82–1.03) | 0.84 ± 0.03 (0.78–0.89) | 0.24 |
| | radD [× 10–3 mm2 s-1] | | | axD [× 10–3 mm2 s-1] | | | radD [× 10–3 mm2 s-1] | | | axD [× 10–3 mm2 s-1] | | |
| CC | 0.70 ± 0.08 (0.61–0.82) | 0.60 ± 0.05 (0.53–0.67) | 0.005 | 1.66 ± 0.10 (1.56–1.86) | 1.57 ± 0.07 (1.45–1.71) | 0.36 | 0.73 ± 0.11 (0.56–0.87) | 0.60 ± 0.04 (0.55–0.69) | 0.004 | 1.57 ± 0.10 (1.37–1.70) | 1.40 ± 0.05 (1.34–1.50) | < 0.001 |
| CC Genu | 0.68 ± 0.08 (0.56–0.79) | 0.64 ± 0.06 (0.55–0.76) | 1.00 | 1.51 ± 0.11 (1.37–1.66) | 1.50 ± 0.10 (1.37–1.74) | 1.00 | 0.70 ± 0.10 (0.55–0.84) | 0.66 ± 0.06 (0.58–0.78) | 1.00 | 1.43 ± 0.10 (1.26–1.57) | 1.35 ± 0.07 (1.25–1.47) | 0.28 |
| CC Body | 0.71 ± 0.08 (0.62–0.86) | 0.61 ± 0.05 (0.53–0.68) | 0.02 | 1.59 ± 0.10 (1.50–1.82) | 1.51 ± 0.07 (1.39–1.66) | 0.70 | 0.73 ± 0.12 (0.57–0.95) | 0.60 ± 0.04 (0.54–0.71) | 0.01 | 1.53 ± 0.14 (1.32–1.80) | 1.33 ± 0.05 (1.26–1.42) | < 0.001 |
| CC Splenium | 0.73 ± 0.07 (0.63–0.85) | 0.58 ± 0.04 (0.49–0.68) | < 0.001 | 1.83 ± 0.11 (1.73–2.06) | 1.64 ± 0.07 (1.53–1.78) | < 0.001 | 0.70 ± 0.12 (0.59–1.03) | 0.61 ± 0.03 (0.56–0.68) | 0.23 | 1.68 ± 0.14 (1.48–1.97) | 1.45 ± 0.06 (1.35–1.58) | < 0.001 |
| L Cingulum | 0.70 ± 0.07 (0.63–0.81) | 0.62 ± 0.04 (0.51–0.69) | 0.03 | 1.26 ± 0.05 (1.19–1.33) | 1.24 ± 0.04 (1.18–1.32) | 1.00 | 0.71 ± 0.06 (0.65–0.81) | 0.67 ± 0.04 (0.61–0.75) | 0.62 | 1.20 ± 0.04 (1.15–1.27) | 1.16 ± 0.04 (1.10–1.24) | 0.39 |
| R Cingulum | 0.72 ± 0.07 (0.64–0.83) | 0.63 ± 0.04 (0.55–0.68) | 0.01 | 1.26 ± 0.07 (1.19–1.39) | 1.21 ± 0.04 (1.14–1.27) | 1.00 | 0.71 ± 0.06 (0.60–0.81) | 0.66 ± 0.03 (0.61–0.72) | 0.15 | 1.17 ± 0.05 (1.07–1.24) | 1.12 ± 0.03 (1.07–1.17) | 0.11 |
| L ILF | 0.68 ± 0.08 (0.60–0.87) | 0.60 ± 0.04 (0.54–0.69) | 0.07 | 1.37 ± 0.07 (1.22–1.46) | 1.28 ± 0.06 (1.18–1.40) | 0.10 | 0.67 ± 0.05 (0.61–0.77) | 0.62 ± 0.04 (0.54–0.69) | 0.20 | 1.32 ± 0.06 (1.21–1.41) | 1.23 ± 0.04 (1.18–1.32) | 0.003 |
| R ILF | 0.68 ± 0.04 (0.62–0.74) | 0.60 ± 0.05 (0.53–0.68) | 0.02 | 1.33 ± 0.04 (1.25–1.36) | 1.22 ± 0.07 (1.09–1.34) | 0.04 | 0.67 ± 0.06 (0.61–0.80) | 0.63 ± 0.04 (0.56–0.70) | 0.69 | 1.29 ± 0.05 (1.21–1.38) | 1.24 ± 0.05 (1.18–1.33) | 0.89 |
| L SLF | 0.64 ± 0.04 (0.56–0.71) | 0.58 ± 0.04 (0.48–0.65) | 0.03 | 1.22 ± 0.04 (1.18–1.29) | 1.18 ± 0.04 (1.09–1.25) | 0.37 | 0.64 ± 0.05 (0.58–0.73) | 0.57 ± 0.03 (0.53–0.62) | 0.001 | 1.16 ± 0.03 (1.12–1.21) | 1.10 ± 0.03 (1.04–1.16) | < 0.001 |
| R SLF | 0.68 ± 0.06 (0.60–0.75) | 0.58 ± 0.03 (0.51–0.65) | < 0.001 | 1.25 ± 0.05 (1.21–1.34) | 1.17 ± 0.04 (1.13–1.24) | 0.003 | 0.66 ± 0.06 (0.57–0.78) | 0.59 ± 0.02 (0.56–0.63) | 0.01 | 1.16 ± 0.04 (1.07–1.22) | 1.11 ± 0.03 (1.05–1.15) | 0.02 |
| L UNC | 0.64 ± 0.04 (0.57–0.69) | 0.63 ± 0.06 (0.57–0.83) | 1.00 | 1.29 ± 0.04 (1.24–1.36) | 1.28 ± 0.04 (1.22–1.37) | 1.00 | 0.71 ± 0.06 (0.60–0.80) | 0.67 ± 0.04 (0.60–0.77) | 0.69 | 1.25 ± 0.07 (1.14–1.37) | 1.20 ± 0.05 (1.10–1.31) | 0.98 |
| R UNC | 0.65 ± 0.04 (0.58–0.73) | 0.63 ± 0.07 (0.55–0.79) | 1.00 | 1.30 ± 0.04 (1.24–1.35) | 1.26 ± 0.06 (1.12–1.38) | 1.00 | 0.69 ± 0.06 (0.64–0.86) | 0.65 ± 0.04 (0.60–0.72) | 0.57 | 1.24 ± 0.06 (1.18–1.39) | 1.20 ± 0.03 (1.14–1.25) | 0.18 |

Values are means ± standard deviations. P values refer to ANCOVA model adjusted for age and Bonferroni-corrected for multiple comparisons. Abbreviations: axD = axial diffusivity; CC = corpus callosum; FA = fractional anisotropy; HC = healthy controls; ILF = inferior longitudinal fasciculus; L = left; MD = mean diffusivity; PCA = posterior cortical atrophy; R = right; radD = radial diffusivity; SLF = superior longitudinal fasciculus; UNC = uncinate fasciculus.

**Table 4**
Regions of decreased resting state functional connectivity in PCA patients compared with healthy controls.

| Sample#1 | | | | | | Sample#2 | | | | | |
|---|---|---|---|---|---|---|---|---|---|---|---|
| Region | Cluster extent | x | y | z | Z | Region | Cluster extent | x | y | z | Z |
| Visual I network | | | | | | Visual I network | | | | | |
| R Calcarine | 142 | 6 | −94 | 4 | 4.66 | L Precuneus | 41 | −10 | −58 | 44 | 2.95 |
| L Calcarine | | −2 | −86 | 0 | 4.01 | R Precuneus | | 6 | −70 | 48 | 2.94 |
| L Cuneus | | −2 | −90 | 24 | 3.60 | L Middle occipital | 24 | −34 | −86 | 28 | 3.73 |
| R Cuneus | | 2 | −86 | 36 | 3.45 | R Precuneus | 3 | 2 | −42 | 56 | 3.04 |
| L Middle occipital | 11 | −54 | −74 | 4 | 4.78 | L Precuneus | 1 | −6 | −58 | 60 | 3.03 |
| L Inferior occipital | | −50 | −74 | −4 | 3.54 | | | | | | |
| R Middle temporal | 5 | 38 | −58 | 8 | 3.69 | | | | | | |
| Default mode network | | | | | | Default mode network | | | | | |
| R Calcarine | 415 | 10 | −62 | 12 | 5.58 | R Precuneus | 64 | 6 | −50 | 20 | 4.10 |
| L Superior occipital | | −22 | −66 | 36 | 5.27 | R Posterior cingulum | | 2 | −38 | 16 | 3.38 |
| L Lingual | | −10 | −46 | 0 | 4.48 | | | | | | |
| L Cuneus | | −2 | −70 | 32 | 4.45 | | | | | | |
| R Precuneus | | 6 | −54 | 24 | 3.92 | | | | | | |
| R Posterior cingulum | | 14 | −46 | 28 | 3.74 | | | | | | |
| L Middle temporal | 94 | −46 | −54 | 20 | 4.42 | | | | | | |
| L Middle occipital | | −42 | −70 | 12 | 3.48 | | | | | | |
| L Middle occipital | 9 | −50 | −78 | 36 | 3.75 | | | | | | |
| Dorsal attentive network | | | | | | Right frontoparietal network | | | | | |
| L Paracentral lobule | 8 | −2 | −26 | 56 | 5.41 | R Supramarginal | 8 | 54 | −42 | 40 | 4.18 |
| L Superior temporal | 3 | −58 | −34 | 20 | 4.98 | R Inferior parietal | 1 | 46 | −50 | 52 | 4.40 |
| L Supramarginal | 1 | −58 | −26 | 20 | 4.09 | | | | | | |
| Salience network | | | | | | | | | | | |
| L Thalamus | 7 | −10 | −22 | 8 | 4.72 | | | | | | |
| L Hippocampus | | −14 | −34 | 8 | 3.88 | | | | | | |
| Frontal network | | | | | | | | | | | |
| R Anterior cingulum | 125 | 6 | 46 | 20 | 4.19 | | | | | | |
| R Medial superior frontal | | 2 | 42 | 44 | 3.83 | | | | | | |
| L Anterior cingulum | | −2 | 26 | 24 | 3.52 | | | | | | |

Coordinates (x, y, z) are in Montreal Neurological Institute space. Results are shown at $p < 0.05$ family-wise error corrected for multiple comparisons. Abbreviations: L = left; R = right.

related with neuronal degeneration of the posterior brain cortices. ILF involvement, due to its crucial role in carrying the visual information from occipital areas to the temporal lobe (Catani et al., 2003), is likely to contribute to deficits such as object recognition, prosopagnosia and/or alexia (Epelbaum et al., 2008; Ffytche et al., 2010; Simon et al., 2011). Damage of the SLF, which links the parietal lobes to the frontal brain regions (Catani et al., 2002), may be related to the patient dorsal symptoms, such as the altered detection of object locations, neglect and optic ataxia (Andrade et al., 2010; Doricchi et al., 2008). Furthermore, SLF involvement together with that of the body of CC (with fibers projecting to the motor regions) may be associated with the ideomotor apraxia present in some of our cases (Catani and Ffytche, 2005). Finally, in both samples we observed changes in the splenium of the CC that could be associated not only with visuospatial but also with memory deficits (Rudge and Warrington, 1991).

Functional connectivity was affected in both the visual network and posterior regions of the DMN in patients with PCA regardless the clinical stage. Findings on the visual network are in agreement with two previous RS fMRI studies of PCA (Lehmann et al., 2015; Migliaccio et al., 2016), supporting the early involvement of syndrome-specific brain networks in AD variants (Lehmann et al., 2013; Ossenkoppele et al., 2015). We observed a decreased functional connectivity in the posterior cortical hubs of the DMN, according to its central role across AD phenotypes (Lehmann et al., 2015; Lehmann et al., 2013; Ossenkoppele et al., 2015). A correspondence between regions of GM atrophy in PCA patients and posterior-DMN functional connectivity map derived from healthy subjects has been reported (Lehmann et al., 2013; Ossenkoppele et al., 2015). Contrary to previous studies (Lehmann et al., 2015; Migliaccio et al., 2016), we did not find areas of increased DMN connectivity in PCA patients relative to controls. Hyperconnectivity, which has been previously observed also in typical late-onset AD (Agosta et al., 2012; Damoiseaux et al., 2012), has been attributed to multiple pathophysiological factors (Hillary et al., 2015) including aberrant communication in response to brain damage and neural resilience during the initial stage of brain dysfunction which usually disappears with the disease progression. The variability of clinical data and structural damage amount among study samples may explain the lack or the presence of increased connectivity patterns in the fMRI literature of AD.

The observation of findings obtained in our two PCA samples may help elucidating trajectories of disease spreading. In agreement with previous studies (Caso et al., 2015; Madhavan et al., 2016; Migliaccio et al., 2012b; Migliaccio et al., 2012c), DT MRI showed more extensive changes than expected purely due to the posterior atrophy seen on structural imaging. In addition, PCA patients with longer disease duration and greater disease severity showed further WM damage to the cingulum as well as decreased functional connectivity in the frontal, salience, and dorsal-attentive networks. All together, these findings may provide evidence that disease targets posterior DMN and visual (syndrome-specific) network simultaneously at onset. According to the network-based degeneration hypothesis (Seeley et al., 2009), neurodegeneration spreading in PCA may then rapidly involve lateral parieto-temporal cortices and finally follow posterior-to-anterior pathways to reach most distant frontal cortical hubs and basal ganglia. The distributed WM damage observed in our patients suggests that pathology may propagate stepwise through CC and long-distance structural connections such as the cingulum, ILF and SLF. As a support of this latter, in both our samples we observed that the reduced DMN functional connectivity was associated with structural alterations of the right SLF and left ILF. Obviously, a better understanding of the evolution of the

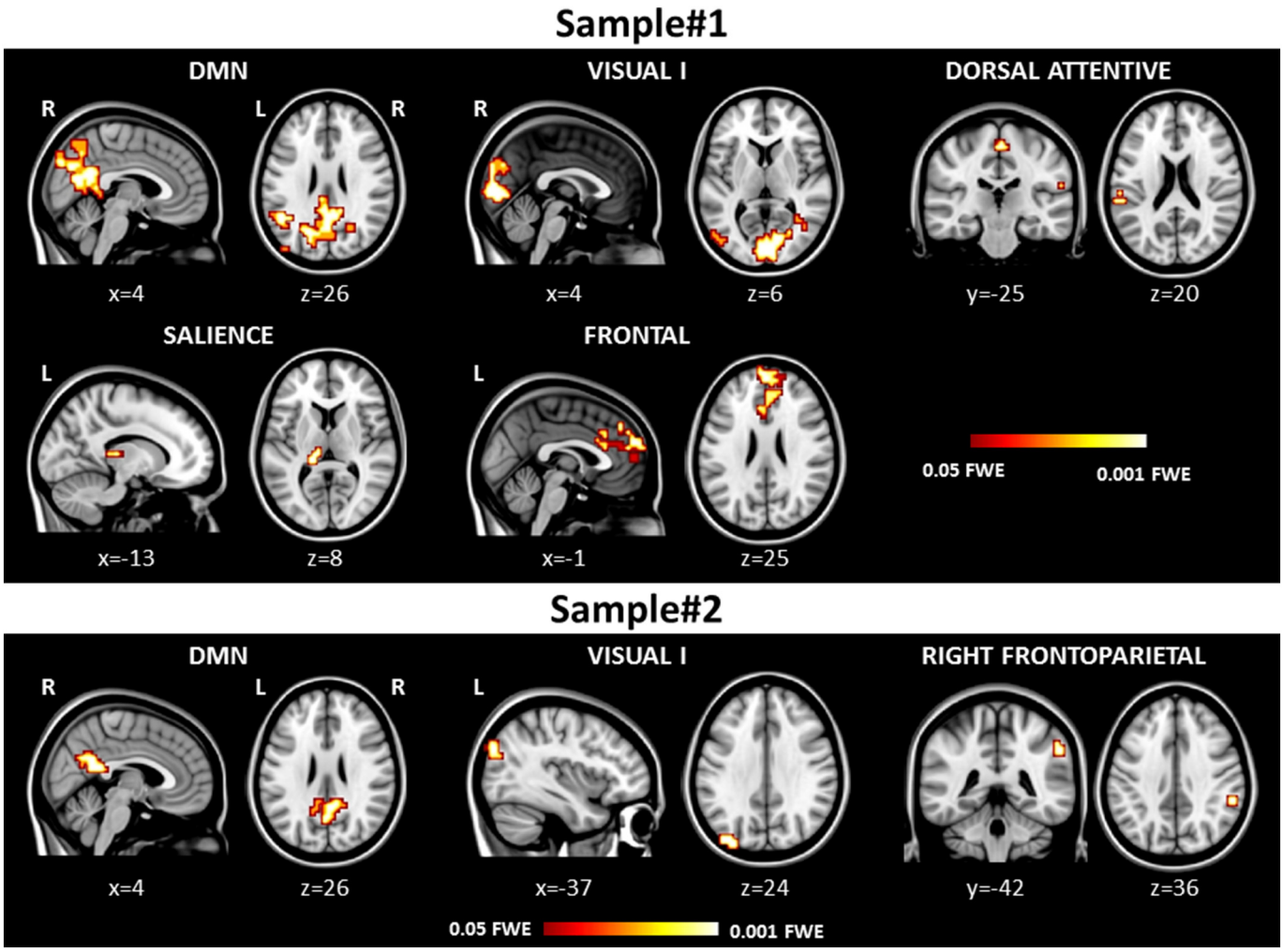


**Fig. 2.** Reduced resting state functional connectivity in the investigated networks in patients with posterior cortical atrophy compared with healthy controls accounting for age and grey matter atrophy. Results are overlaid on the Montreal Neurological Institute standard brain in neurological convention (right is right), and displayed at $p < 0.05$ family-wise error (FWE) corrected for multiple comparisons. Coloured bars represent p values.

disease requires longitudinal studies. In a cognitively normal research volunteer who developed a ventral phenotype of PCA and was followed up for 5 years, structural MRI analysis revealed atrophy which was initially most marked in inferior temporal and posterior parietal cortices before spreading to occipital cortices and subsequently to more anterior regions (Kennedy et al., 2012).

Although clinical differences are our first explanation for different MRI findings between patient populations, we cannot exclude that they are due to heterogeneity in terms of underneath pathology. In this study, we provided AD biomarkers for the majority of cases. However, as suggested by the last consensus classification for PCA (Crutch et al., 2017), alternative pathologies such as corticobasal degeneration and Lewy body disease could be the cause of neurodegeneration in PCA cases leading to different patterns of damage. In addition, different MR scanners and magnetic field strengths (1.5 vs 3 T) may have affected findings in distinct ways with 1.5 T having higher risk of false positive results due to a worse signal to noise ratio (SNR) but 3.0 T being characterized by an increased level of artifacts. While it is unlikely that 1.5 and 3 T scans did significantly differ in their power to detect GM atrophy patterns on T1-weighted images (Ho et al., 2010), the increased SNR at 3.0 T should have been resulted in smaller variances in estimated DT MRI parameters (Alexander et al., 2006). Indeed, although the amount of EPI distortion roughly doubled going from 1.5 T to 3.0 T, it is reduced by 50% when using parallel imaging as in our protocol (Alexander et al., 2006). In addition, higher fields should also result in improved sensitivity and spatial specificity for detection of fMRI signal (Triantafyllou et al., 2005).

Some additional methodological shortcomings should be considered when interpreting our data. An important caveat is the lack of pathological confirmation for the clinical diagnosis. However, a multidisciplinary panel of clinicians, experts in the field, evaluated all patients. In addition, for the majority of patients, the clinical diagnosis was biomarker-supported thus increasing diagnostic certainty, at least for the underneath AD pathology. Second, this is a cross-sectional study. Third, although we replicated similar findings in two independent samples, overall sample size is still relatively small and this is probably the reason why we did not observe a significant association between MRI alterations and clinical features.

To conclude, in two independent samples of PCA patients, we showed distributed WM damage suggesting DT MRI as a potential adjunct in the early diagnosis of PCA. Moreover, altered RS functional connectivity extends with disease worsening from occipital to temporoparietal and frontostriatal regions, and we speculated that this may likely occur through WM connections. Future larger and longitudinal studies are needed to verify our hypotheses on damage spreading in PCA and establish whether a combined DT MRI/RS fMRI approach is promising in monitoring the disease progression.

## Funding

This study has been supported by the Italian Ministry of Health and Regione Lombardia (#GR-2010-2303035 and #GR-2011-02351217), the Alzheimer's Drug Discovery Foundation(#20131211), and the Ministry of Education and Science, Republic of Serbia (project #175090).

## Disclosure statement

F. Agosta is Section Editor of *NeuroImage: Clinical*; has received speaker honoraria from Biogen Idec and Novartis; and receives research supports from the Italian Ministry of Health, AriSLA (Fondazione Italiana di Ricerca per la SLA), and the European Research Council.

G. Mandic-Stojmenovic, T. Stojković, F. Imperiale, F. Caso, and E. Stefanova report no disclosures.

E. Canu has received research support from the Italian Ministry of Health.

M. Copetti has received compensation for consulting and/or serving on advisory boards from Teva Pharmaceuticals and Biogen Idec.

V. Kostic has received research grants from Ministry of Education and Science, Republic of Serbia and the Serbian Academy of Science and Arts; he receives research supports from Valeant, Stada, Novartis and Boehriner Ingelheim, and speaker honoraria from Novartis and Boehringer Ingelheim.

M. Filippi is Editor-in-Chief of *Journal of Neurology*; received compensation for consulting services and/or speaking activities from Biogen Idec, Merck-Serono, Novartis, Teva Pharmaceutical Industries; and receives research support from Biogen Idec, Merck-Serono, Novartis, Teva Pharmaceutical Industries, Roche, Italian Ministry of Health, Fondazione Italiana Sclerosi Multipla, and ARiSLA (Fondazione Italiana di Ricerca per la SLA).

## Appendix A. Supplementary data

Supplementary data to this article can be found online at https://doi.org/10.1016/j.nicl.2018.06.013.

## References

Agosta, F., Pievani, M., Geroldi, C., Copetti, M., Frisoni, G.B., Filippi, M., 2012. Resting state fMRI in Alzheimer's disease: beyond the default mode network. Neurobiol. Aging 33, 1564–1578.

Alexander, A.L., Lee, J.E., Wu, Y.C., Field, A.S., 2006. Comparison of diffusion tensor imaging measurements at 3.0 T versus 1.5 T with and without parallel imaging. Neuroimaging Clin. N. Am. 16, 299–309 (xi).

Alladi, S., Xuereb, J., Bak, T., Nestor, P., Knibb, J., Patterson, K., Hodges, J.R., 2007. Focal cortical presentations of Alzheimer's disease. Brain 130, 2636–2645.

Andersson, J.L., Jenkinson, M., Smith, S., 2007. Non-linear Registration, Aka Spatial Normalisation. Technical Report. FMRIB Centre, Oxford.

Andrade, K., Samri, D., Sarazin, M., de Souza, L.C., Cohen, L., de Thiebaut Schotten, M., Dubois, B., Bartolomeo, P., 2010. Visual neglect in posterior cortical atrophy. BMC Neurol. 10, 68.

Ashburner, J., 2007. A fast diffeomorphic image registration algorithm. NeuroImage 38, 95–113.

Beckmann, C.F., Deluca, M., Devlin, J.T., Smith, S.M., 2005. Investigations into resting-state connectivity using independent component analysis. Philos. Trans. R. Soc. Lond. Ser. B Biol. Sci. 360, 1001–1013.

Behrens, T.E., Berg, H.J., Jbabdi, S., Rushworth, M.F., Woolrich, M.W., 2007. Probabilistic diffusion tractography with multiple fibre orientations: what can we gain? NeuroImage 34, 144–155.

Borruat, F.X., 2013. Posterior cortical atrophy: review of the recent literature. Curr. Neurol. Neurosci. Rep. 13, 406.

Canu, E., Kostic, M., Agosta, F., Munjiza, A., Ferraro, P.M., Pesic, D., Copetti, M., Peljto, A., Tosevski, D.L., Filippi, M., 2015. Brain structural abnormalities in patients with major depression with or without generalized anxiety disorder comorbidity. J. Neurol. 262, 1255–1265.

Caso, F., Agosta, F., Mattavelli, D., Migliaccio, R., Canu, E., Magnani, G., Marcone, A., Copetti, M., Falautano, M., Comi, G., Falini, A., Filippi, M., 2015. White matter degeneration in atypical Alzheimer disease. Radiology 277, 162–172.

Catani, M., Ffytche, D.H., 2005. The rises and falls of disconnection syndromes. Brain 128, 2224–2239.

Catani, M., Howard, R.J., Pajevic, S., Jones, D.K., 2002. Virtual in vivo interactive dissection of white matter fasciculi in the human brain. NeuroImage 17, 77–94.

Catani, M., Jones, D.K., Donato, R., Ffytche, D.H., 2003. Occipito-temporal connections in the human brain. Brain 126, 2093–2107.

Crutch, S.J., Lehmann, M., Schott, J.M., Rabinovici, G.D., Rossor, M.N., Fox, N.C., 2012. Posterior cortical atrophy. Lancet Neurol. 11, 170–178.

Crutch, S.J., Schott, J.M., Rabinovici, G.D., Murray, M., Snowden, J.S., van der Flier, W.M., Dickerson, B.C., Vandenberghe, R., Ahmed, S., Bak, T.H., Boeve, B.F., Butler, C., Cappa, S.F., Ceccaldi, M., de Souza, L.C., Dubois, B., Felician, O., Galasko, D., Graff-Radford, J., Graff-Radford, N.R., Hof, P.R., Krolak-Salmon, P., Lehmann, M., Magnin, E., Mendez, M.F., Nestor, P.J., Onyike, C.U., Pelak, V.S., Pijnenburg, Y., Primativo, S., Rossor, M.N., Ryan, N.S., Scheltens, P., Shakespeare, T.J., Suarez Gonzalez, A., Tang-Wai, D.F., Yong, K.X., Carrillo, M., Fox, N.C., Alzheimer's Association, I.A.A.s.D., Associated Syndromes Professional Interest, A, 2017. Consensus classification of posterior cortical atrophy. Alzheimers Dement. 13, 870–884.

Damoiseaux, J.S., Prater, K.E., Miller, B.L., Greicius, M.D., 2012. Functional connectivity tracks clinical deterioration in Alzheimer's disease. Neurobiol. Aging 33 (828), e819–e830.

Doricchi, F., de Thiebaut Schotten, M., Tomaiuolo, F., Bartolomeo, P., 2008. White matter (dis)connections and gray matter (dys)functions in visual neglect: gaining insights into the brain networks of spatial awareness. Cortex 44, 983–995.

Epelbaum, S., Pinel, P., Gaillard, R., Delmaire, C., Perrin, M., Dupont, S., Dehaene, S., Cohen, L., 2008. Pure alexia as a disconnection syndrome: new diffusion imaging evidence for an old concept. Cortex 44, 962–974.

Ffytche, D.H., Blom, J.D., Catani, M., 2010. Disorders of visual perception. J. Neurol. Neurosurg. Psychiatry 81, 1280–1287.

Filippini, N., MacIntosh, B.J., Hough, M.G., Goodwin, G.M., Frisoni, G.B., Smith, S.M., Matthews, P.M., Beckmann, C.F., Mackay, C.E., 2009. Distinct patterns of brain activity in young carriers of the APOE-epsilon4 allele. Proc. Natl. Acad. Sci. U. S. A. 106, 7209–7214.

Greve, D.N., Fischl, B., 2009. Accurate and robust brain image alignment using boundary-based registration. NeuroImage 48, 63–72.

Hillary, F.G., Roman, C.A., Venkatesan, U., Rajtmajer, S.M., Bajo, R., Castellanos, N.D., 2015. Hyperconnectivity is a fundamental response to neurological disruption. Neuropsychology 29, 59–75.

Ho, A.J., Hua, X., Lee, S., Leow, A.D., Yanovsky, I., Gutman, B., Dinov, I.D., Lepore, N., Stein, J.L., Toga, A.W., Jack Jr., C.R., Bernstein, M.A., Reiman, E.M., Harvey, D.J., Kornak, J., Schuff, N., Alexander, G.E., Weiner, M.W., Thompson, P.M., 2010. Comparing 3 T and 1.5 T MRI for tracking Alzheimer's disease progression with tensor-based morphometry. Hum. Brain Mapp. 31, 499–514.

Hof, P.R., Vogt, B.A., Bouras, C., Morrison, J.H., 1997. Atypical form of Alzheimer's disease with prominent posterior cortical atrophy: a review of lesion distribution and circuit disconnection in cortical visual pathways. Vis. Res. 37, 3609–3625.

Jenkinson, M., Smith, S., 2001. A global optimisation method for robust affine registration of brain images. Med. Image Anal. 5, 143–156.

Jenkinson, M., Beckmann, C.F., Behrens, T.E., Woolrich, M.W., Smith, S.M., 2012. Fsl. Neuroimage. 62, 782–790.

Kennedy, J., Lehmann, M., Sokolska, M.J., Archer, H., Warrington, E.K., Fox, N.C., Crutch, S.J., 2012. Visualizing the emergence of posterior cortical atrophy. Neurocase 18, 248–257.

Lehmann, M., Crutch, S.J., Ridgway, G.R., Ridha, B.H., Barnes, J., Warrington, E.K., Rossor, M.N., Fox, N.C., 2011. Cortical thickness and voxel-based morphometry in posterior cortical atrophy and typical Alzheimer's disease. Neurobiol. Aging 32, 1466–1476.

Lehmann, M., Madison, C.M., Ghosh, P.M., Seeley, W.W., Mormino, E., Greicius, M.D., Gorno-Tempini, M.L., Kramer, J.H., Miller, B.L., Jagust, W.J., Rabinovici, G.D., 2013. Intrinsic connectivity networks in healthy subjects explain clinical variability in Alzheimer's disease. Proc. Natl. Acad. Sci. U. S. A. 110, 11606–11611.

Lehmann, M., Madison, C., Ghosh, P.M., Miller, Z.A., Greicius, M.D., Kramer, J.H., Coppola, G., Miller, B.L., Jagust, W.J., Gorno-Tempini, M.L., Seeley, W.W., Rabinovici, G.D., 2015. Loss of functional connectivity is greater outside the default mode network in nonfamilial early-onset Alzheimer's disease variants. Neurobiol. Aging 36, 2678–2686.

Levine, D.N., Lee, J.M., Fisher, C.M., 1993. The visual variant of Alzheimer's disease: a clinicopathologic case study. Neurology 43, 305–313.

Madhavan, A., Schwarz, C.G., Duffy, J.R., Strand, E.A., Machulda, M.M., Drubach, D.A., Kantarci, K., Przybelski, S.A., Reid, R.I., Senjem, M.L., Gunter, J.L., Apostolova, L.G., Lowe, V.J., Petersen, R.C., Jack, C.R., Josephs, K.A., Whitwell, J.L., 2016. Characterizing white matter tract degeneration in syndromic variants of Alzheimer's disease: a diffusion tensor imaging study. J. Alzheimers Dis. 49, 633–643.

Mendez, M.F., Ghajarania, M., Perryman, K.M., 2002. Posterior cortical atrophy: clinical characteristics and differences compared to Alzheimer's disease. Dement. Geriatr. Cogn. Disord. 14, 33–40.

Migliaccio, R., Agosta, F., Rascovsky, K., Karydas, A., Bonasera, S., Rabinovici, G.D., Miller, B.L., Gorno-Tempini, M.L., 2009. Clinical syndromes associated with posterior atrophy: early age at onset AD spectrum. Neurology 73, 1571–1578.

Migliaccio, R., Agosta, F., Possin, K.L., Rabinovici, G.D., Miller, B.L., Gorno-Tempini, M.L., 2012a. White matter atrophy in Alzheimer's disease variants. Alzheimers Dement. 8 (S78–87), e71–e72.

Migliaccio, R., Agosta, F., Scola, E., Magnani, G., Cappa, S.F., Pagani, E., Canu, E., Comi, G., Falini, A., Gorno-Tempini, M.L., Bartolomeo, P., Filippi, M., 2012b. Ventral and dorsal visual streams in posterior cortical atrophy: a DT MRI study. Neurobiol. Aging 33, 2572–2584.

Migliaccio, R., Agosta, F., Toba, M.N., Samri, D., Corlier, F., de Souza, L.C., Chupin, M., Sharman, M., Gorno-Tempini, M.L., Dubois, B., Filippi, M., Bartolomeo, P., 2012c. Brain networks in posterior cortical atrophy: a single case tractography study and

literature review. Cortex 48, 1298–1309.
Migliaccio, R., Gallea, C., Kas, A., Perlbarg, V., Samri, D., Trotta, L., Michon, A., Lacomblez, L., Dubois, B., Lehericy, S., Bartolomeo, P., 2016. Functional connectivity of ventral and dorsal visual streams in posterior cortical atrophy. J. Alzheimers Dis. 51, 1119–1130.
Nestor, P.J., Caine, D., Fryer, T.D., Clarke, J., Hodges, J.R., 2003. The topography of metabolic deficits in posterior cortical atrophy (the visual variant of Alzheimer's disease) with FDG-PET. J. Neurol. Neurosurg. Psychiatry 74, 1521–1529.
Nichols, T.E., Holmes, A.P., 2002. Nonparametric permutation tests for functional neuroimaging: a primer with examples. Hum. Brain Mapp. 15, 1–25.
Ossenkoppele, R., Cohn-Sheehy, B.I., La Joie, R., Vogel, J.W., Moller, C., Lehmann, M., van Berckel, B.N., Seeley, W.W., Pijnenburg, Y.A., Gorno-Tempini, M.L., Kramer, J.H., Barkhof, F., Rosen, H.J., van der Flier, W.M., Jagust, W.J., Miller, B.L., Scheltens, P., Rabinovici, G.D., 2015. Atrophy patterns in early clinical stages across distinct phenotypes of Alzheimer's disease. Hum. Brain Mapp. 36, 4421–4437.
Pruim, R.H., Mennes, M., van Rooij, D., Llera, A., Buitelaar, J.K., Beckmann, C.F., 2015. ICA-AROMA: a robust ICA-based strategy for removing motion artifacts from fMRI data. NeuroImage 112, 267–277.
Rohde, G.K., Barnett, A.S., Basser, P.J., Marenco, S., Pierpaoli, C., 2004. Comprehensive approach for correction of motion and distortion in diffusion-weighted MRI. Magn. Reson. Med. 51, 103–114.
Rudge, P., Warrington, E.K., 1991. Selective impairment of memory and visual perception in splenial tumours. Brain 114 (Pt 1B), 349–360.
Seeley, W.W., Crawford, R.K., Zhou, J., Miller, B.L., Greicius, M.D., 2009. Neurodegenerative diseases target large-scale human brain networks. Neuron 62, 42–52.
Seguin, J., Formaglio, M., Perret-Liaudet, A., Quadrio, I., Tholance, Y., Rouaud, O., Thomas-Anterion, C., Croisile, B., Mollion, H., Moreaud, O., Salzmann, M., Dorey, A., Bataillard, M., Coste, M.H., Vighetto, A., Krolak-Salmon, P., 2011. CSF biomarkers in posterior cortical atrophy. Neurology 76, 1782–1788.
Simon, S.R., Khateb, A., Darque, A., Lazeyras, F., Mayer, E., Pegna, A.J., 2011. When the brain remembers, but the patient doesn't: converging fMRI and EEG evidence for covert recognition in a case of prosopagnosia. Cortex 47, 825–838.
Smith, S.M., Nichols, T.E., 2009. Threshold-free cluster enhancement: addressing problems of smoothing, threshold dependence and localisation in cluster inference. NeuroImage 44, 83–98.
Smith, S.M., Jenkinson, M., Woolrich, M.W., Beckmann, C.F., Behrens, T.E., Johansen-Berg, H., Bannister, P.R., De Luca, M., Drobnjak, I., Flitney, D.E., Niazy, R.K., Saunders, J., Vickers, J., Zhang, Y., De Stefano, N., Brady, J.M., Matthews, P.M., 2004. Advances in functional and structural MR image analysis and implementation as FSL. NeuroImage 23 (Suppl. 1), S208–S219.
Smith, S.M., Fox, P.T., Miller, K.L., Glahn, D.C., Fox, P.M., MacKay, C.E., Filippini, N., Watkins, K.E., Toro, R., Laird, A.R., Beckmann, C.F., 2009. Correspondence of the brain's functional architecture during activation and rest. Proc. Natl. Acad. Sci. U. S. A. 106, 13040–13045.
Tang-Wai, D.F., Graff-Radford, N.R., Boeve, B.F., Dickson, D.W., Parisi, J.E., Crook, R., Caselli, R.J., Knopman, D.S., Petersen, R.C., 2004. Clinical, genetic, and neuropathologic characteristics of posterior cortical atrophy. Neurology 63, 1168–1174.
Triantafyllou, C., Hoge, R.D., Krueger, G., Wiggins, C.J., Potthast, A., Wiggins, G.C., Wald, L.L., 2005. Comparison of physiological noise at 1.5 T, 3 T and 7 T and optimization of fMRI acquisition parameters. NeuroImage 26, 243–250.
Whitwell, J.L., Jack Jr., C.R., Kantarci, K., Weigand, S.D., Boeve, B.F., Knopman, D.S., Drubach, D.A., Tang-Wai, D.F., Petersen, R.C., Josephs, K.A., 2007. Imaging correlates of posterior cortical atrophy. Neurobiol. Aging 28, 1051–1061.
Whitwell, J.L., Graff-Radford, J., Singh, T.D., Drubach, D.A., Senjem, M.L., Spychalla, A.J., Tosakulwong, N., Lowe, V.J., Josephs, K.A., 2017. 18F-FDG PET in posterior cortical atrophy and dementia with Lewy bodies. J. Nucl. Med. 58, 632–638.
Woolrich, M.W., Jbabdi, S., Patenaude, B., Chappell, M., Makni, S., Behrens, T., Beckmann, C., Jenkinson, M., Smith, S.M., 2009. Bayesian analysis of neuroimaging data in FSL. NeuroImage 45, S173–S186.